A Langenberg et al.

Prospects of X-ray Imaging Spectrometers for Impurity Transport: Recent Results from the Stellarator Wendelstein 7-X

Preprint of Paper to be submitted for publication in Proceeding of 18th Topical Conference on High Temperature Plasma Diagnostics (HTPD)

Prospects of X-ray Imaging Spectrometers for Impurity Transport: Recent Results from the Stellarator Wendelstein 7-X[a]

A. Langenberg,[1, b] N.A. Pablant,[2] Th. Wegner,[1] P. Traverso,[3] O. Marchuk,[4] T. Bräuer,[1] B. Geiger,[1] G. Fuchert,[1] S. Bozhenkov,[1] E. Pasch,[1] O. Grulke,[1] F. Kunkel,[1] C. Killer,[1] D. Nicolai,[4] G. Satheeswaran,[4] K.P. Hollfeld,[4] B. Schweer,[4] T. Krings,[4] P. Drews,[4] G. Offermanns,[4] A. Pavone,[1] J. Svensson,[1] J.A. Alonso,[5] R. Burhenn,[1] R.C. Wolf,[1] and the W7-X Team[c]

[1] *Max-Planck-Institut für Plasmaphysik, 17491 Greifswald, Germany*

[2] *Princeton Plasma Physics Laboratory, Princeton, NJ, USA*

[3] *Auburn University, Auburn, Alabama, USA*

[4] *Forschungszentrum Jülich GmbH, Institut für Energie- und Klimaforschung - Plasmaphysik, 52425 Jülich, Germany*

[5] *Laboratorio Nacional de Fusión, Asociación EURATOM-CIEMAT, Madrid, Spain*

(Dated: 7 May 2018)

This paper reports on the design and the performance of the recently upgraded X-ray imaging spectrometer systems XICS and HR-XIS, installed at the optimized stellarator Wendelstein 7-X (W7-X). High resolution spectra of highly ionized, He-like Si, Ar, Ti, and Fe as well as H-like Ar have been observed. A cross comparison of ion and electron temperature profiles derived from a spectral fit and tomographic inversion of Ar and Fe spectra shows a reasonable match comparing both spectrometers. The also measured impurity density profiles of Ar and Fe have peaked densities at radial positions that are in qualitative agreement with expectations from the He-like impurity fractional abundances, given the measured temperature profiles. Repeated measurements of impurity decay times have been demonstrated with an accuracy of 1 ms via injection of non-recycling Ti, Fe, and Mo impurities using a laser blow-off system.

PACS numbers: Valid PACS appear here

I. INTRODUCTION

X-ray imaging crystal spectrometers are widely used on large scale fusion devices[1–7] for routine measurements of ion and electron temperatures, T_i and T_e, and plasma flows v_p, but have also been used for estimations of the neutral hydrogen density in plasmas[8,9], for the detection of up down asymmetries in the argon emission at Alcator C-Mod[10,11], and for monitoring the impurity emission during impurity injection experiments[12–14]. In latter experiments, trace amounts of impurities are injected into the plasma and either the temporal or the combined spatio-temporal impurity emission is recorded using several diagnostics, providing impurity decay times[13–15] and impurity transport parameters from a comparison with transport code calculations[16–25]. Compared to other diagnostics, X-ray imaging spectrometers are particular well suited for impurity transport investigations for several reasons: On the one hand, their high resolution allows precise measurements of the radial electric field[26–28], being a critical parameter in stellarators as its radial profile determines different transport regimes, *e.g.* ion or electron root confinement[29,30]. On the other hand, the

selectivity of imaging spectrometers to a single impurity species in a particular charge state allows for a direct measurement of impurity fluxes and impurity transport parameters, as recently shown for Ar impurities[12]. Moreover, the time resolution of high end X-ray detectors of 2-10 ms is small compared to typical confinement times and the use of commercial available large area X-ray detectors allows to design viewing geometries of the spectrometer, covering a large area of the plasma cross section.

In order to allow systematic studies on the confinement of impurities of different atomic numbers Z as well as for an extension of the accessible temperature range, the X-ray imaging crystal spectrometer (XICS) and the high resolution X-ray imaging spectrometer (HR-XIS) diagnostics have been equipped with 8 additional crystals. This paper gives an overview on the design and calibration of XICS and HR-XIS (Sec.II), shows observed impurity spectra, reports on the commissioning and cross calibration of both diagnostics (Sec.III), and gives an outlook for the application of X-ray imaging spectrometers for impurity transport studies (Sec.IV), based on results obtained at W7-X.

II. IMAGING SPECTROMETERS XICS AND HR-XIS

A. Design Parameters

The XICS and HR-XIS diagnostics use spherical bent crystals to image the X-ray emission of impurities emitted from the plasma onto a two dimensional detector
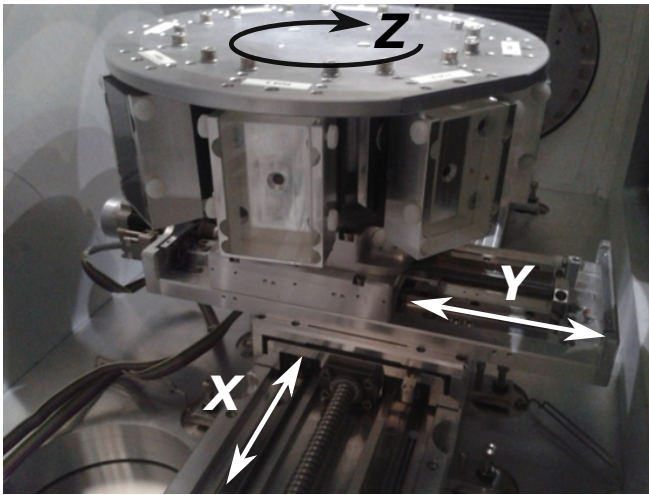

FIG. 1. The movable (x and y direction) and rotatable (around z axis) crystal table of the HR-XIS diagnostic with its 8 crystal holders for installation of various crystals for X-ray diffraction. The crystal table diameter measures 310 mm.
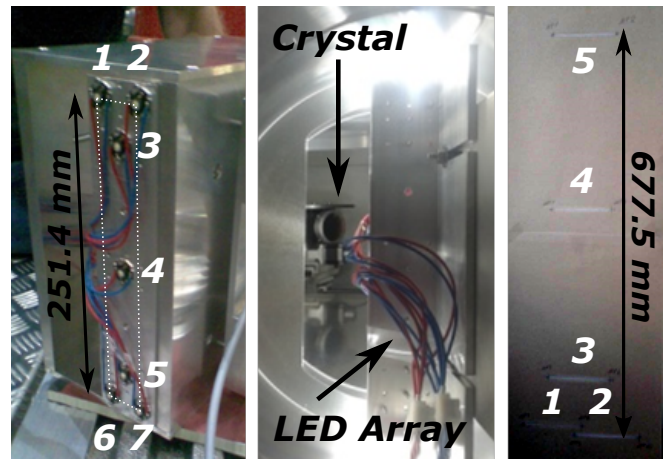

FIG. 2. Left: LED array with dimensions of the detector unit (dashed line) for the back illumination of the spectrometer lines of sight. Middle: LED array installed at the detector position, illuminating the crystal. Right: Spectrometer lines of sight projected onto a target placed at the sagittal focus.

System	Crystal (Cut)	Bragg Angle	Impurity
XICS	Quartz (11-20)	53.90 °	Ar^{16+}
	Quartz (10-12)	54.83 °	Ar^{17+}
			Fe^{24+}
			Mo^{32+}
HR-XIS	Quartz (-1100)	51.88 °	Si^{12+}
	Quartz (11-20)	53.90 °	Ar^{16+}
	Quartz (11-20)	49.39 °	Ar^{17+}
	Silicon (311)	53.22 °	Ti^{20+}
	Germanium (422)	53.61 °	Fe^{24+}
	Germanium (440)	52.95 °	Ni^{26+}
	Silicon (531)	54.00 °	Cu^{27+}
	Germanium (533)	51.96 °	W^{64+}

TABLE I. Overview on crystals, crystal cuts, Bragg angles, and observable spectra of impurity species in particular charge states for the XICS and HR-XIS diagnostic.

plane with energy and spatial resolution along the horizontal and vertical direction on the detector, respectively. The basic diagnostic layout as well as initial measurements of XICS and HR-XIS, obtained during the first operational phase of W7-X (OP1.1), have been reported in[12,26,31–33]. For the second operational phase (OP1.2a), both spectrometers have been upgraded with additional crystals and detector units for the measurement of additional impurity species in various charge states with atomic numbers ranging from $Z=14$ up to $Z=74$. All crystals are rectangular with an area of 40×100 mm^2 (XICS) or 40×85 mm^2 (HR-XIS), have a thickness of $\geq$ 20 μm and are placed onto spherical shaped glass substrates with Rowland circle diameters of approximately 3.1 m. Table I lists the crystals, crystal cuts, Bragg an-

gles, and observable spectra of impurity species in particular charge states for the XICS and HR-XIS diagnostics. XICS is equipped with two quartz crystals and two detector units (Dectris, Pilatus300K-W). For a simultaneous observation of He- and H-like argon, both crystals are placed on one substrate that has been cut into two pieces which are tilted away from each other by 2.5 degrees in the horizontal direction. This way, an overlap of H- and He-like Ar emission lines on one detector is avoided and H- and He-like Ar spectra can be imaged well separated onto the two side by side installed detector units[33] with identical line of sight viewing geometries for both systems. In addition, Ne-like Mo emission lines in first order and He-like Fe lines in second order can be monitored. The detectors use a hybrid pixel technology, combining a two dimensional pixelated Si sensor with an array of readout channels designed with an advanced complementary metal-oxide-semiconductor technology for single photon detection without dark current or readout noise[34].

The original layout of the HR-XIS diagnostic goes back to a design described by Bertschinger[35]. As foreseen in the design, now HR-XIS has been equipped with multiple crystals, namely two quartz, two silicon, three germanium crystals, and one detector unit (Dectris, Pilatus300K-W). For positioning, crystals are mounted on a rotatable and movable crystal table, shown in Fig.1. The rotation around the z axis (see Fig.1) allows to choose one crystal and adjust the Bragg angle according to Tab.I. The x direction for the crystal table movement has been chosen to be in line with the spectrometer lines of sight. Thus, an adjustment of the crystal table in x direction allows for setting different Bragg angles while keeping the spectrometer lines of sight directions unchanged[35]. Movement of the table in y direction allows to adjust the focal position of the imaged spectra on the detector[9]. The crystal table can be controlled re-

motely and every crystal position can be set within 10 s.

B. Spatial Calibration

For the spatial calibration of the spectrometers viewing geometries, the line of sight paths have been back illuminated using a light emitting diode (LED) array, mounted at the detector positions of both spectrometers.

The front side of the LED array is shown in Fig.2 on the left. It consists of 7 high flux LEDs (*Seoul Z-LED P4*), each providing 240 lm. The 4 outermost LEDs are arranged in a rectangle with dimensions identical to the active detector area, see left side of Fig.2, dotted lines. Additional 3 LEDs are aligned horizontally centered across the imitated detector area.

The LEDs act as point sources for visible light, illuminating the polished crystal surface (see middle of Fig.2) that itself focuses the light into 7 cone shaped lines of sight being identical to the spectrometer lines of sight for imaging X-rays. The right side of Fig.2 shows the projection of 5 lines of sight onto a target, placed at the position of the sagittal focus. Due to the imaging properties of the crystal, the upper LEDs 1 and 2 correspond to the lowest lines of sight and vice versa. The actual detector surface position, the crystal position, and the projected line of sight positions are measured in 3D using a laser tracker outside as well as inside the plasma vessel that allows to define the absolute positions of the outermost lines of sight inside the plasma vessel for both spectrometers with an accuracy of ± 1.5 mm. Given a spatial resolution of 2 cm for an individual line of sight, this method yields a very accurate spatial line of sight calibration.

III. COMMISSIONING OF XICS AND HR-XIS

A. Overview of Observed Impurity Spectra

Fig.3 shows an overview of observed He- and H-like spectra, measured using different crystals as listed in Tab.I. The Si, Ti, and Fe impurities were injected using a laser blow-off (LBO) system[36], Ar was injected by a gas puff. All spectra are measured along the central line of sight of the spectrometers[12] and the given count rates have been averaged for 200 ms after an impurity injection.

In the He-like spectra, the main excitation lines w, x, y, z, the dielectronic satellites k and $n \geq 3$, and the most prominent satellites from inner shell excitations q, r, s, a have been labeled. All spectra are shown including the Bremsstrahlung radiation background. For the He-like Ar and Fe spectra, spectral fits are shown as thin solid black lines and the residuals, defined as deviation between measured and fitted spectra, are shown as dotted lines. Except for the Fe x and z emission lines, the spectral fits match the measured spectra along the entire
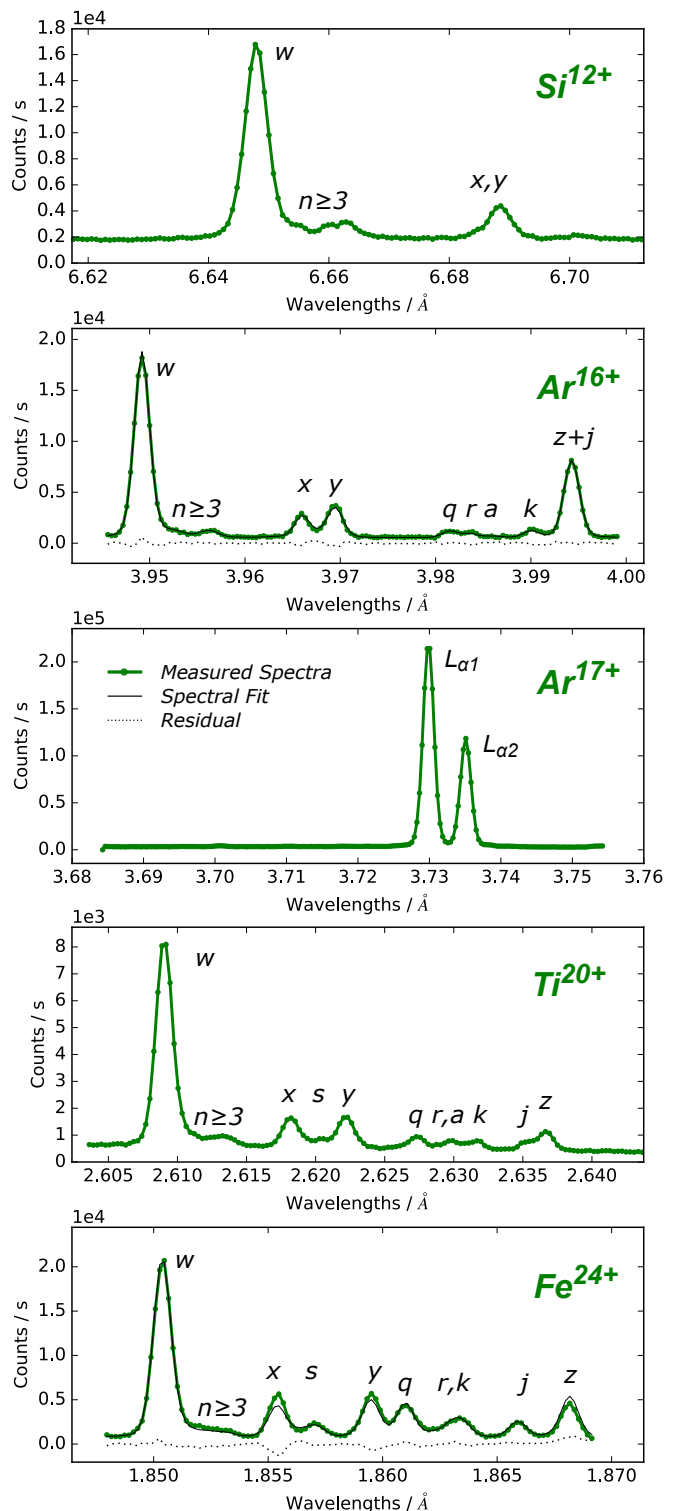

FIG. 3. Spectra of He- and H-like impurities inside W7-X plasmas measured along the central spectrometer line of sight for atomic numbers ranging from $Z=14$ to $Z=26$. Ar impurities were recorded by the XICS system, Si, Ti, and Fe impurities by the HR-XIS diagnostic. Spectral fits are shown as thin solid lines together with the residual in dotted lines.

Impurity	Experiment ID	n_e / 1×10^{19}m^{-3}	$T_{i/e}$ / keV
Si^{12+}	171011.055 @ 0.8 s	-	
Ar^{16+}	171004.049 @ 2.0 s	-	T_e=1.9±0.1
			T_i=1.8±0.1
Ar^{17+}	171108.021 @ 0.6 s	1.5±0.1	
Ti^{20+}	171011.045 @ 1.3 s	1.3±0.1	
Fe^{24+}	171011.039 @ 0.7 s	1.0±0.1	T_e=4.3±0.2
			T_i=1.9±0.1

TABLE II. Documentation for experiment program numbers, line of sight averaged electron densities, and fitted, line averaged temperatures of spectra shown in Fig.3.

spectrum within the statistical uncertainties.

Since the gas inlet valves used for Ar injection are absolutely calibrated, the total amount of injected Ar particles can be estimated to $N_{Ar} = 8.8\times10^{17}$ ($n_{Ar}/n_e = 1.8\times10^{-4}$). The amount of ablated material from the glass plates of the LBO system can be estimated from the metal coating thickness, the laser spot diameter and a factor accounting for the fraction of neutrals reaching the plasma to a value of injected Ti and Fe particles in the order of $N_{Ti/Fe} \approx 10^{16}$ ($n_Z/n_e \approx 0.5\times10^{-4}$). The quality of the observed spectra, given the low impurity content, underline the high sensitivity of X-ray imaging spectrometers to even trace amounts of impurities.

Table II lists for the individual spectra of Fig.3 the W7-X program numbers, the measured averaged electron density n_e from the interferometer diagnostic[31], and if available, T_i and T_e obtained from the spectral fits. Here, T_i has been derived from the Doppler broadening of lines and T_e from line intensity ratios, fitting all line intensities of the entire spectrum[7].

B. XICS / HR-XIS Temperature Profile Validation

Although the XICS and HR-XIS diagnostics are installed at different toroidal positions with different viewing geometries[7] and usually observe different impurity species, the tomographic inverted T_i and T_e profiles inferred from both spectrometer data are expected to be identical for a given experiment program. For a validation, two experiment programs with Ar and Fe injections were performed and for program 171004.049, both spectrometers were set to observe Ar while for the program 171122.022, HR-XIS was set to observe Fe while XICS monitored the Ar impurity emission. In Fig.4, the inferred T_i and T_e profiles using tomographic inversion[12] as well as impurity density profiles are shown along the plasma radius ρ, here defined as the square root of the magnetic flux ψ, normalized to the flux of the last closed flux surface: $\rho = \sqrt{\psi/\psi_{LCFS}}$. Solid and dashed lines represent profiles inverted from HR-XIS and XICS data, shaded areas mark the uncertainties of the inverted profiles within a statistical width of one standard deviation

1σ.

The determined T_i profiles in Fig.4 of both spectrometers match each other within the 1σ uncertainty along the entire plasma radius comparing the Ar-Ar as well as the Ar-Fe impurity measurements. In case of the Ar-Ar comparison (Fig.4, top left), measured T_i profiles show an excellent match between $\rho = 0.2-0.5$, with uncertainties of $\Delta T_i = 0.1$ keV. Towards the plasma edge, the uncertainties in the T_i profiles significantly rise for $\rho \geq 0.6$ (HR-XIS) and $\rho \geq 0.85$ (XICS), directly related to the outermost line of sight positions of $\rho = 0.65$ for HR-XIS and $\rho = 0.85$ for XICS. As expected, outside the viewing geometry of the spectrometers, a change in the widths of spectral lines does not significantly affect the observed spectra. Indeed, first the signal I drops rapidly due to the low plasma density ($I \propto n_e$). Second, at electron temperatures below 0.5 keV the excitation rate coefficient of the w line reduces dramatically[37].

The measured T_e profiles also show a reasonable match comparing Ar-Ar and Ar-Fe data, although for individual radial positions the match is not within the 1σ but within the 2σ uncertainties (not shown). For the Ar-Ar data, T_e profiles close to the plasma center deviate from each other by 0.9 keV accompanied by increased uncertainties of $\Delta T_e = \pm0.5$ keV. Both effects are induced by the observed hollow $n_{Ar^{16+}}$ profile (see Fig.4, left T_e and $n_{Ar^{16+}}$ profiles), causing a significantly reduced signal level I in the plasma center ($I \propto n_{Ar^{16+}}$). The low Ar^{16+} concentration in the plasma center originates from a strong reduced fractional abundances of He-like Ar for electron temperatures above 3 keV[38] and is expected to be further enhanced by the central electron root confinement present in centrally electron cyclotron resonance heated W7-X plasmas for given T_e and n_e values[26] driving out impurities from the plasma center by a positive radial electric field[27,29].

For a determination of $n_{Ar^{16+}}$ and $n_{Fe^{24+}}$ profiles from measured absolute line intensities of the XICS spectra, the electron density profile n_e needs to be known and has been taken from Thomson scattering measurements[39,40]. The inferred $n_{Ar^{16+}}$ and $n_{Fe^{24+}}$ profiles shown in the right bottom panel of Fig.4 have peaked densities at $\rho = 0.5$ for Ar and $\rho = 0.2$ for Fe, being in qualitative agreement with the fractional abundances of Ar^{16+} and Fe^{24+} charge states at the given T_e profile.

IV. IMPURITY TRANSPORT STUDIES

In this paragraph, initial results from the measurements of impurity decay times using HR-XIS in combination with a laser blow-off system are discussed. Impurities were injected into a stationary phase of an experiment program, when T_e and n_e profiles were constant. The time traces of the HR-XIS signals shown in Fig.6 correspond to the measured w line intensity I_w of impurity spectra, accumulated along the entire HR-XIS view field and are proportional to the He-like impurity density.

XICS / HR-XIS Profiles, Program 20171004.049 @2.0 s
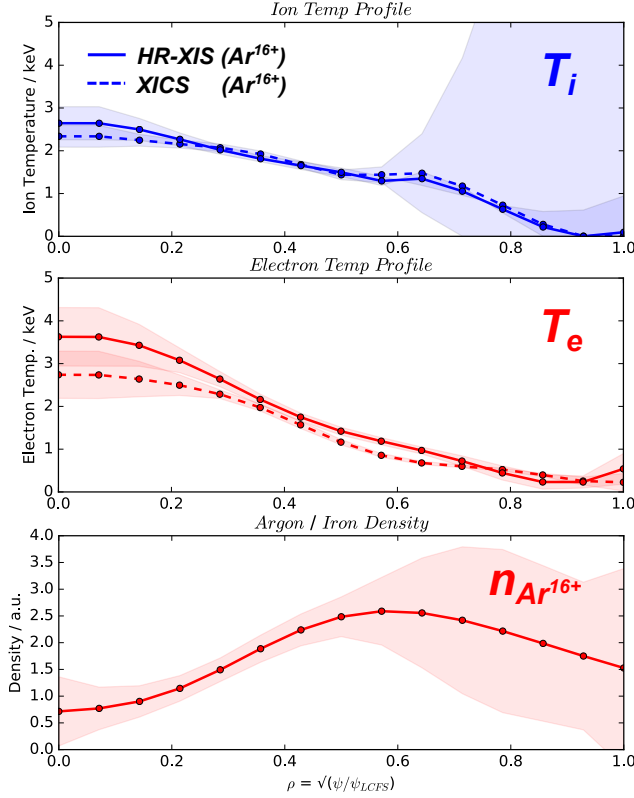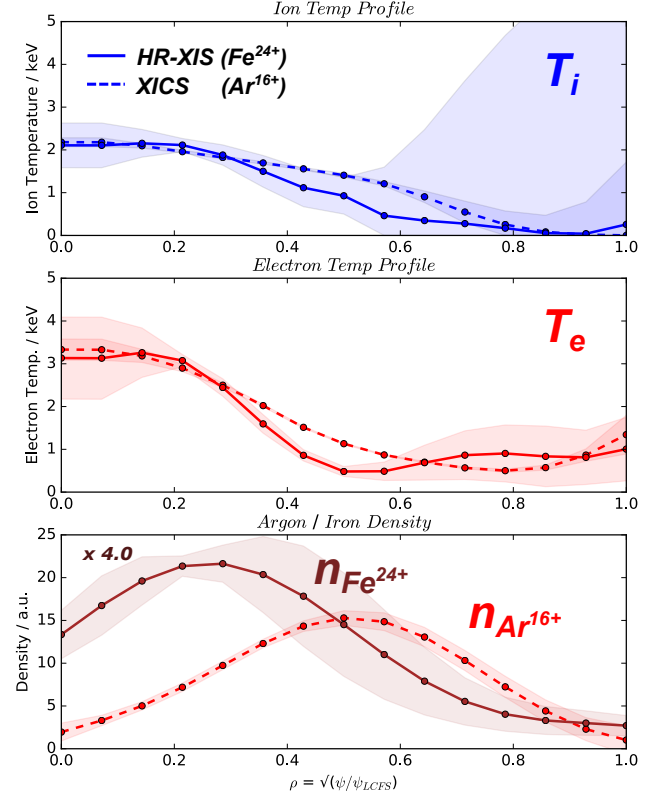
XICS / HR-XIS Profiles, Program 20171122.022 @2.6 s

FIG. 4. Comparison of inverted temperature and impurity density profiles from the HR-XIS (solid lines) and the XICS (dashed lines) diagnostics. Left: Both spectrometers observing Ar. Right: HR-XIS observing Fe and XICS observing Ar impurities.
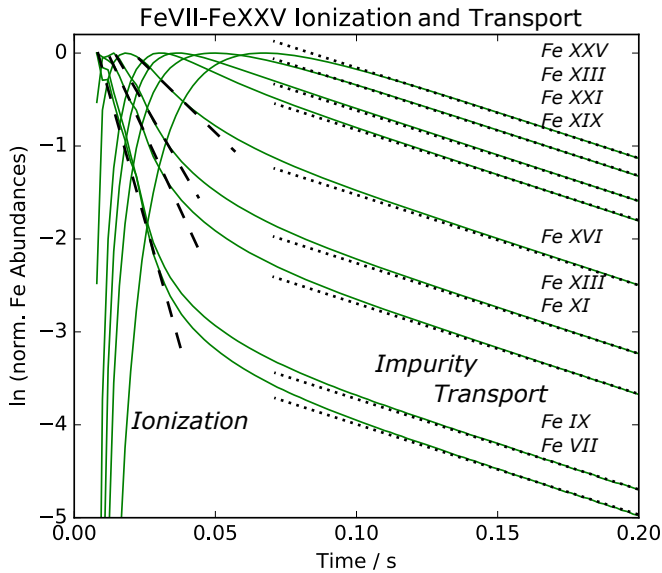
FeVII-FeXXV Ionization and Transport

FIG. 5. Simulated temporal evolution of FeVII - FeXXV charge states after a pulsed iron injection, see text.

A.   Definition of Time Constants

After the injection of neutral impurity species into a hot plasma, impurities are transported into the plasma and are sequentially ionized from low towards high ionization states within ionization times τ_{ion} being different for the individual ionization states. In order to get an estimation of involved time constants, the temporal behavior of such an ionization process has been simulated with the transport code STRAHL[41] for a pulsed Fe impurity injection by LBO, central temperatures and densities of $T_e(0) = 2.7$ keV and $n_e(0)=8.5\times10^{19}$ m^{-3} and assumed transport parameters[12] of $v = 0$ m/s and $D = 1.0\ m^2/s$. The result is shown in Fig.5 for FeVII-FeXXV charge state abundances on a logarithmic scale. Right after the injection, especially the low ionization states decay with a fast time constant caused by the ionization into higher charge states in regions of increasing temperature towards the plasma center, see dashed lines in Fig.5. After the establishment of an equilibrium distribution, the observed decay times become stationary for all ionization states (see Fig.5, dotted lines) reflecting the impurity transport properties. This time constant has been denoted as the impurity transport time τ_i throughout this paper, representing a measure which is related
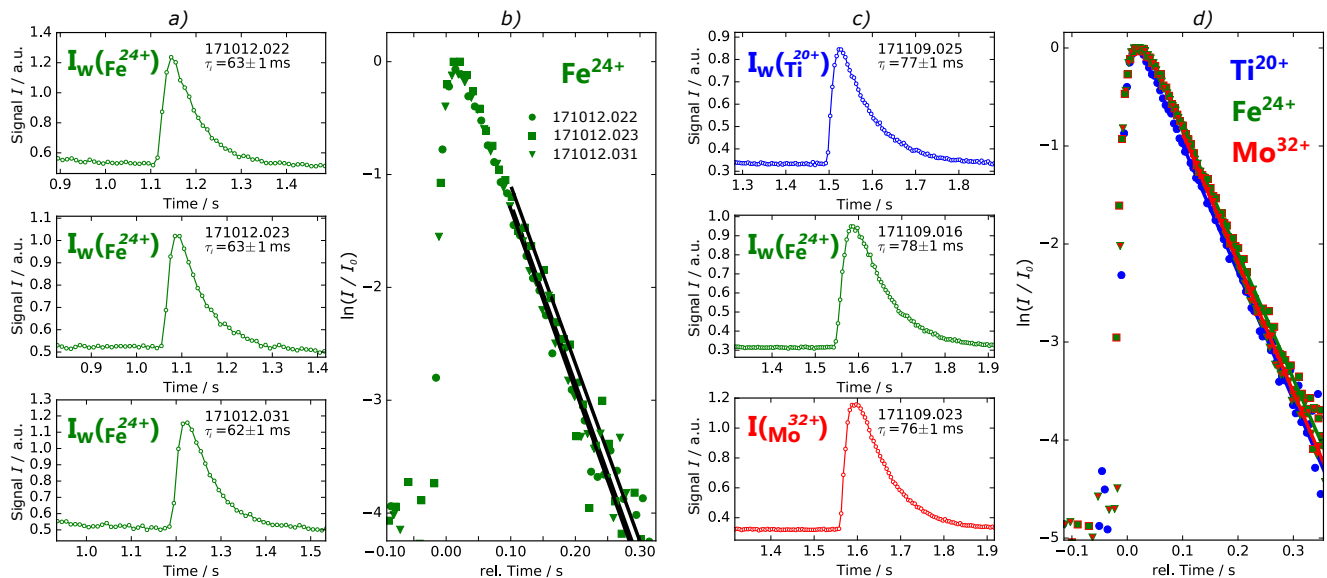
FIG. 6. Time traces of Ti^{20+}, Fe^{24+}, and Mo^{32+} line brightnesses I_w after impurity injections using the laser blow-off system: a) Repeated injections of Fe into identical experiment programs. b) Logarithmic plot of normalized Fe^{24+} time traces from a) and linear fits of the impurity transport times (solid lines). c) Injections of Ti, Fe, and Mo impurities into identical experiment programs. d) Logarithmic plot of normalized Ti^{20+}, Fe^{24+}, and Mo^{32+} time traces from c) and linear fits of the impurity transport times (solid lines).

to the impurity confinement properties of the plasma[36].

B. Measurement of Impurity Transport Times

Figure 6 a) shows time traces of $n_{Fe^{24+}}$ (green circles) for three repeated, identical experiment programs at central plasma parameters of $T_e(0)$=4.3 keV and $n_e(0)$=1.4×10^{19} m^{-3}. Using the LBO system, the Fe injection has been realized at about 1.1 s, clearly visible as peaks in the density time traces. Fig.6 b) shows a logarithmic plot of all three density time traces of Fig.6 a) together with a linear fit of the impurity transport time τ_i. As evident, the measured $n_{Fe^{24+}}$ density time traces as well as the fitted transport times show a high reproducibility with $\Delta\tau_i = \pm 1$ ms.

C. Z dependance of Impurity Confinement

Figure 6 c) and d) shows time traces of various impurity densities for repeated, identical experiment programs at central plasma parameters of $T_e(0)$=2.6 keV and $n_e(0)$=8.5×10^{19} m^{-3} for the W7-X magnetic standard configuration EIM^{42}. Since τ_i increases with decreasing heating power and increasing n_e[43], the measured impurity transport time for Fe^{24+} in Fig.6 c) ($\tau_i = 78$ ms) significantly exceeds the value obtained in Fig.6 a) ($\tau_i = 63$ ms). The experiment programs shown in Fig.6 c) and d) aimed to investigate a possible Z dependance on the impurity confinement. Therefore, the

available different crystals of HR-XIS have been used to monitor time traces of Ti^{20+}, Fe^{24+}, and Mo^{32+} impurity densities as shown in Fig.6 c)+d). As can be seen, the obtained transport times of $\tau_i(Ti^{20+})$=77±1 ms, $\tau_i(Fe^{24+})$=78±1 ms, and $\tau_i(Mo^{32+})$=76±1 ms are identical within the experimental errors and doesn't show a clear trend for highly ionized charge states, neither with the impurity charge nor with the charge to mass ratio ranging from 0.43 to 0.33. These findings are comparable to observations made in Tokamak and Heliotron experiments[13,44]. Detailed investigations of Z-dependant transport are planned for the future, including low as well as high Z impurities and scanning non standard magnetic configurations of W7-X.

V. SUMMARY AND OUTLOOK

In this paper, the commissioning of the XICS and HR-XIS diagnostics has been reviewed, showing measured spectra of highly charged Si, Ar, Ti, and Fe impurities, including spectral fits for Ar and Fe data. A comparison of tomographic inverted T_i, T_e, and impurity density profiles shows a reasonable match between both spectrometers for Ar and Fe impurities. Measurements of impurity transport times τ_i can be carried out with a precision of $\Delta\tau_i = \pm 1.0$ ms and in the W7-X magnetic standard configuration, similar impurity transport times have been observed for Ti^{20+}, Fe^{24+}, and Mo^{32+} impurity species.

The ability of imaging spectrometers to provide spa-

tial (Fig.4) and temporal resolved impurity emissivities (Fig.6) provides a broad source of measured data to be compared with transport code simulations using *e.g.* STRAHL[41] for a determination of impurity transport parameters through a variation of D and v profiles with respect to an optimal match between modeled (Fig.5) and measured transport times (Fig.6). Alternatively, the observation of He-like impurity spectra allows in combination with the also accessible neighbored ionization stages evaluations of impurity fluxes[12] that can be used for a validation of neoclassical and turbulent transport, as predicted from calculations, also with respect to the influence of the radial electric field[26] in stellarators. Summing up, X-ray imaging spectrometers can provide widespread experimental data for systematic and comprehensive impurity transport studies in large scale fusion devices.

VI. ACKNOWLEDGMENTS

[1] B. Lyu, J. Chen, R. J. Hu, F. D. Wang, Y. Y. Li, J. Fu, Y. C. Shen, M. Bitter, K. W. Hill, L. F. Delgado-Aparicio, N. Pablant, S. G. Lee, M. Y. Ye, Y. J. Shi, and B. N. Wan, Review of Scientific Instruments **87**, 11E326 (2016), https://aip.scitation.org/doi/pdf/10.1063/1.4960504.

[2] M. L. Reinke, Y. A. Podpaly, M. Bitter, I. H. Hutchinson, J. E. Rice, L. Delgado-Aparicio, C. Gao, M. Greenwald, K. Hill, N. T. Howard, A. Hubbard, J. W. Hughes, N. Pablant, A. E. White, and S. M. Wolfe, Review of Scientific Instruments **83**, 113504 (2012), http://dx.doi.org/10.1063/1.4758281.

[3] Y. Shi, F. Wang, B. Wan, M. Bitter, S. Lee, J. Bak, K. Hill, J. Fu, Y. Li, W. Zhang, A. Ti, and B. Ling, Plasma Physics and Controlled Fusion **52**, 085014 (2010).

[4] A. Ince-Cushman, J. E. Rice, M. Bitter, M. L. Reinke, K. W. Hill, M. F. Gu, E. Eikenberry, C. Broennimann, S. Scott, Y. Podpaly, S. G. Lee, and E. S. Marmar, Review of Scientific Instruments **79**, 10E302 (2008).

[5] S. G. Lee, J. W. Yoo, Y. S. Kim, U. W. Nam, and M. K. Moon, Review of Scientific Instruments **87**, 11E314 (2016), https://aip.scitation.org/doi/pdf/10.1063/1.4960491.

[6] N. A. Pablant, M. Bitter, L. Delgado-Aparicio, M. Goto, K. W. Hill, S. Lazerson, S. Morita, A. L. Roquemore, D. Gates, D. Monticello, H. Nielson, A. Reiman, M. Reinke, J. E. Rice, and H. Yamada, Review of Scientific Instruments **83**, 083506 (2012).

[7] A. Langenberg, J. Svensson, H. Thomsen, O. Marchuk, N. A. Pablant, R. Burhenn, and R. C. Wolf, Fusion Science and Technology **69**, 560 (2016), http://dx.doi.org/10.13182/FST15-181.

[8] J. E. Rice, E. S. Marmar, J. L. Terry, E. Kallne, and J. Kallne, Phys. Rev. Lett. **56**, 50 (1986).

[9] T. Schlummer, *Charge exchange recombination in X-ray spectra of He-like argon measured at the tokamak TEXTOR*, Ph.D. thesis, Heinrich Heine Universität Düsseldorf (2015).

[10] M. Reinke, J. Rice, I. Hutchinson, M. Greenwald, N. Howard, J. Hughes, J. Irby, Y. Podpaly, J. Terry, and A. White, Nuclear Fusion **53**, 043006 (2013).

[11] J. Rice, J. Terry, E. Marmar, and F. Bombarda, Nuclear Fusion **37**, 241 (1997).

[12] A. Langenberg, N. Pablant, O. Marchuk, D. Zhang, J. Alonso, R. Burhenn, J. Svensson, P. Valson, D. Gates, M. Beurskens, R. Wolf, and the W7-X Team, Nuclear Fusion **57**, 086013 (2017).

[13] J. Rice, M. Reinke, C. Gao, N. Howard, M. Chilenski, L. Delgado-Aparicio, R. Granetz, M. Greenwald, A. Hubbard, J. Hughes, J. Irby, Y. Lin, E. Marmar, R. Mumgaard, S. Scott, J. Terry, J. Walk, A. White, D. Whyte, S. Wolfe, and S. Wukitch, Nuclear Fusion **55**, 033014 (2015).

[14] J. E. Rice, J. L. Terry, E. S. Marmar, R. S. Granetz, M. J. Greenwald, A. E. Hubbard, J. H. Irby, S. M. Wolfe, and T. S. Pedersen, Fusion Science and Technology **51**, 357 (2007).

[15] M. Mattioli, R. Giannella, R. Myrnas, C. Demichelis, B. Denne-Hinnov, T. D. D. Wit, and G. Magyar, Nuclear Fusion **35**, 1115 (1995).

[16] K. Zhang, Z.-Y. Cui, P. Sun, C.-F. Dong, W. Deng, Y.-B. Dong, S.-D. Song, M. Jiang, Y.-G. Li, P. Lu, and Q.-W. Yang, Chinese Physics B **25**, 065202 (2016).

[17] J. Arevalo, J. A. Alonso, K. J. McCarthy, and J. L. Velasco, Nuclear Fusion **53**, 023003 (2013).

[18] S. Menmuir, L. Carraro, A. Alfier, F. Bonomo, A. Fassina, G. Spizzo, and N. Vianello, Plasma Physics and Controlled Fusion **52**, 095001 (2010).

[19] M. Leigheb, M. Romanelli, L. Gabellieri, L. Carraro, M. Mattioli, C. Mazzotta, M. E. Puiatti, L. Lauro-Taroni, M. Marinucci, S. Nowak, L. Panaccione, V. Pericoli, P. Smeulders, O. Tudisco, C. Sozzi, M. Valisa, and the FTU team, Plasma Physics and Controlled Fusion **49**, 1897 (2007).

[20] O. Marchuk, M. Z. Tokar, G. Bertschinger, A. Urnov, H. . J. Kunze, D. Pilipenko, X. Loozen, D. Kalupin, D. Reiter, A. Pospieszczyk, W. Biel, M. Goto, and F. Goryaev, Plasma Physics and Controlled Fusion **48**, 1633 (2006).

[21] R. Burhenn, J. Baldzuhn, R. Brakel, H. Ehmler, L. Giannone, P. E. Grigull, J. Knauer, M. Krychowiak, M. Hirsch, K. Ida, H. Maassberg, G. K. McCormick, E. Pasch, H. Thomsen, A. Wel, W.-A. Team, E. Group, and N. Group, Fusion Science and Technology **46**, 115 (2004), https://doi.org/10.13182/FST04-A547.

[22] N. Tamura, S. Sudo, K. V. Khlopenkov, S. Kato, V. Y. Sergeev, S. Muto, K. Sato, H. Funaba, K. Tanaka, T. Tokuzawa, I. Yamada, K. Narihara, Y. Nakamura, K. Kawahata, N. Ohyabu, O. Motojima, and L. experimental groups, Plasma Physics and Controlled Fusion **45**, 27 (2003).

[23] L. Delgado-Aparicio, D. Stutman, K. Tritz, M. Finkenthal, S. Kaye, R. Bell, R. Kaita, B. LeBlanc, F. Levinton, J. Menard, S. Paul, D. Smith, and H. Yuh, Nuclear Fusion **49**, 085028 (2009).

[24] M. E. Puiatti, M. Mattioli, G. Telesca, M. Valisa, I. Coffey, P. Dumortier, C. Giroud, L. C. Ingesson, K. D. Lawson, G. Maddison, A. M. Messiaen, P. Monier-Garbet, A. Murari, M. F. F. Nave, J. Ongena, J. Rapp, J. Strachan, B. Unterberg, M. von Hellermann, and contributors to the EFDA-JET Workprogramme, Plasma Physics and Controlled Fusion **44**, 1863 (2002).

[25] R. Dux, A. Peeters, A. Gude, A. Kallenbach, R. Neu, and A. U. Team, Nuclear Fusion **39**, 1509 (1999).

[26] N. A. Pablant, A. Langenberg, A. Alonso, C. D. Beidler, M. Bitter, S. Bozhenkov, R. Burhenn, M. Beurskens, L. Delgado-Aparicio, A. Dinklage, G. Fuchert, D. Gates, J. Geiger, K. W. Hill, U. Höfel, M. Hirsch, J. Knauer, A. Krämer-Flecken, M. Landreman, S. Lazerson, H. Maaßberg, O. Marchuk, S. Massidda, G. H. Neilson, E. Pasch, S. Satake, J. Svennson, P. Traverso, Y. Turkin, P. Valson, J. L. Velasco, G. Weir, T. Windisch, R. C. Wolf, M. Yokoyama, D. Zhang, and W.-X. Team, Physics of Plasmas **25**, 022508 (2018), https://doi.org/10.1063/1.4999842.

[27] A. Dinklage, C. Beidler, P. Helander, G. Fuchert, H. Maassberg, K. Rahbarnia, T. Sunn Pedersen, and Y. Turkin, "Magnetic configuration effects on the wendelstein 7-x stellarator," Accepted for publication in Nature Physics.

[28] R. Wolf, A. Ali, A. Alonso, J. Baldzuhn, C. Beidler, M. Beurskens, C. Biedermann, H.-S. Bosch, S. Bozhenkov, and R. Brakel, Nuclear Fusion **57**, 102020 (2017).

[29] P. Helander, Reports on Progress in Physics **77**, 087001 (2014).

[30]K. Ida, T. Minami, Y. Yoshimura, A. Fujisawa, C. Suzuki, S. Okamura, S. Nishimura, M. Isobe, H. Iguchi, K. Itoh, S. Kado, Y. Liang, I. Nomura, M. Osakabe, C. Takahashi, K. Tanaka, and K. Matsuoka, Phys. Rev. Lett. **86**, 3040 (2001).

[31]M. Krychowiak, A. Adnan, A. Alonso, T. Andreeva, J. Baldzuhn, T. Barbui, M. Beurskens, W. Biel, C. Biedermann, B. D. Blackwell, H. S. Bosch, S. Bozhenkov, R. Brakel, T. Bräuer, B. B. de Carvalho, R. Burhenn, B. Buttenschön, A. Cappa, G. Cseh, A. Czarnecka, A. Dinklage, P. Drews, A. Dzikowicka, F. Effenberg, M. Endler, V. Erckmann, T. Estrada, O. Ford, T. Fornal, H. Frerichs, G. Fuchert, J. Geiger, O. Grulke, J. H. Harris, H. J. Hartfuß, D. Hartmann, D. Hathiramani, M. Hirsch, U. Höfel, S. Jablonski, M. W. Jakubowski, J. Kaczmarczyk, T. Klinger, S. Klose, J. Knauer, G. Kocsis, R. König, P. Kornejew, A. Kramer-Flecken, N. Krawczyk, T. Kremeyer, I. Ksiazek, M. Kubkowska, A. Langenberg, H. P. Laqua, M. Laux, S. Lazerson, Y. Liang, S. C. Liu, A. Lorenz, A. O. Marchuk, S. Marsen, V. Moncada, D. Naujoks, H. Neilson, O. Neubauer, U. Neuner, H. Niemann, J. W. Oosterbeek, M. Otte, N. Pablant, E. Pasch, T. S. Pedersen, F. Pisano, K. Rahbarnia, L. Ryc, O. Schmitz, S. Schmuck, W. Schneider, T. Schröder, H. Schuhmacher, B. Schweer, B. Standley, T. Stange, L. Stephey, J. Svensson, T. Szabolics, T. Szepesi, H. Thomsen, J.-M. Travere, H. T. Mora, H. Tsuchiya, G. M. Weir, U. Wenzel, A. Werner, B. Wiegel, T. Windisch, R. Wolf, G. A. Wurden, D. Zhang, A. Zimbal, and S. Zoletnik, Review of Scientific Instruments **87**, 11D304 (2016), http://aip.scitation.org/doi/pdf/10.1063/1.4964376.

[32]H. Thomsen, R. Burhenn, A. Langenberg, G. Bertschinger, C. Biedermann, W. Biel, B. Buttenschön, M. Kubkowska, O. Marchuk, N. Pablant, L. Ryc, D. Zhang, K. Grosser, and T. Pedersen, Proceedings of Science **1** (2015).

[33]N. A. Pablant, M. Bitter, R. Burhenn, L. Delgado-Aparicio, R. Ellis, D. Gates, M. Goto, K. W. Hill, A. Langenberg, S. Lazerson, M. Mardenfeld, S. Morita, G. H. Neilson, and T. Oishi, in *41st EPS conference, ECA*, Vol. 38F (2014) p. 1.076.

[34]B. Henrich, A. Bergamaschi, C. Broennimann, R. Dinapoli, E. Eikenberry, I. Johnson, M. Kobas, P. Kraft, A. Mozzanica, and B. Schmitt, Nuclear Instruments and Methods in Physics Research Section A: Accelerators, Spectrometers, Detectors and Associated Equipment **607**, 247 (2009).

[35]G. Bertschinger, W. Biel, H. Jaegers, and O. Marchuk, Review of Scientific Instruments **75**, 3727 (2004).

[36]T. Wegner, B. Geiger, F. Kunkel, R. Burhenn, T. Schröder, C. Biedermann, B. Buttenschön, G. Cseh, P. Drews, O. Grulke, K. Hollfeld, C. Killer, G. Kocsis, T. Krings, A. Langenberg, O. Marchuk, U. Neuner, D. Nicolai, G. Offermanns, N. Pablant, K. Rahbarnia, G. Satheeswaran, J. Schilling, B. Schweer, T. Szepesi, H. Thomsen, and the W7-X Team, "Design, capabilities and first results of the new laser blow-off system on wendelstein 7-x," Submitted for publication to Review of Scientific Instruments.

[37]O. Marchuk, *Modeling of He-like spectra measured at the tokamaks TEXTOR and TORE SUPRA*, Ph.D. thesis, Ruhr Universität Bochum (2004).

[38]P. Bryans, N. R. Badnell, T. W. Gorczyca, J. M. Laming, W. Mitthumsiri, and D. W. Savin, The Astrophysical Journal Supplement Series **167**, 343 (2006).

[39]S. Bozhenkov, M. Beurskens, A. D. Molin, G. Fuchert, E. Pasch, M. Stoneking, M. Hirsch, U. Höfel, J. Knauer, J. Svensson, H. T. Mora, and R. Wolf, Journal of Instrumentation **12**, P10004 (2017).

[40]E. Pasch, M. N. A. Beurskens, S. A. Bozhenkov, G. Fuchert, J. Knauer, R. C. Wolf, and W.-X. Team, Review of Scientific Instruments **87**, 11E729 (2016), https://aip.scitation.org/doi/pdf/10.1063/1.4962248.

[41]R. Dux, *STRAHL user manual*, Max-Planck-Institue for Plasmaphysics (2006), iPP Report 10/30.

[42]T. Andreeva, "Vacuum magnetic configurations of wendelstein 7-x," Tech. Rep. (Max-Planck-Institut für Plasmaphysik, Garching, 2002).

[43]R. Burhenn, Y. Feng, K. Ida, H. Maassberg, K. McCarthy, D. Kalinina, M. Kobayashi, S. Morita, Y. Nakamura, H. Nozato, S. Okamura, S. Sudo, C. Suzuki, N. Tamura, A. Weller, M. Yoshinuma, and B. Zurro, Nuclear Fusion **49**, 065005 (2009).

[44]J. Rice, J. Terry, E. Marmar, O. Motojima, H. Kaneko, K. Kondo, T. Mizuuchi, S. Besshou, T. Mutoh, F. Sano, A. Sasaki, M. Sato, S. Sudo, H. Zushi, M. Iima, K. Magome, T. Obiki, A. Iiyoshi, and K. Uo, Nuclear Fusion **24**, 1205 (1984).